Boundary RG and crossover scaling in surface critical phenomena

Nina Anikeeva
Department of Physics, Massachusetts Institute of Technology, Cambridge, Massachusetts 02139, USA
(Dated: May 14, 2026)

A boundary at bulk criticality introduces an independent scaling field and distinct surface universality classes. We combine the semi-infinite Landau–Ginzburg description, its one-loop boundary RG eigenvalue, and a 3D Ising slab Monte Carlo study with tunable surface coupling J_s to identify the regime where one-parameter boundary scaling collapses correlation data and to diagnose the obstruction to extracting the crossover exponent y_c at accessible sizes. Boundary correlation ratios collapse onto a single horizontal scale across four ordinary-side couplings, both in real space and in momentum space. Binder crossings give a finite-size working estimate $J_s^* = 1.388(13)$ (statistical error only), shifted from the precision simple-cubic value by what is plausibly aspect-ratio drift. A direct fit gives $y_c^{\rm app} \simeq 4.95$, far from the known Ising value near 0.72, which we diagnose as a finite-window failure mode of the local-slope estimator rather than a measurement of the surface universality class.

I. INTRODUCTION

Boundary critical behavior extends bulk universality because a wall allows new local operators and new fixed points: ordinary, special, and extraordinary.[1, 2, 7] The classical picture has been substantially refined since: for $O(N)$ with $2 \le N < N_c$ (with $N_c > 3$), what was historically called the extraordinary fixed point is now understood to be an "extraordinary-log" phase with logarithmically decaying boundary correlations rather than power-law order.[13] The Ising case ($N = 1$) lies outside this window and the standard three-class classification still applies, but the broader landscape is the context for any modern boundary-RG analysis. At bulk criticality, tuning the surface enhancement through the special value produces a crossover length

$$\ell_c \sim |c - c^*|^{-1/y_c}, \tag{1}$$

where y_c is the RG eigenvalue of the boundary thermal scaling field. In Eq. (1) and below, c denotes the *renormalized* scaling field of Eq. (6); the bare c_0 enters only through the matching $c_0 - c_{\rm sp,0} = \mu Z_c c$. Where the bare/renormalized distinction does not affect the conclusion — as in the Gaussian benchmark of Sec. II — we drop the subscript and refer to c loosely. The goal here is to connect this continuum statement to explicit lattice measurements in a 3D Ising slab. The useful distinction is between a structure test, namely whether one boundary scaling field collapses the correlation data, and a precision exponent test, which requires a much broader finite-size window.

This distinction matters because the positive and negative parts of the project have different evidentiary standards. A collapse test asks whether changing the microscopic surface coupling can be absorbed into one emergent length scale. A precision estimate of y_c asks for an asymptotic power law over a range where microscopic corrections and finite-size saturation are both small. The current data are useful for the first question and inadequate for the second.

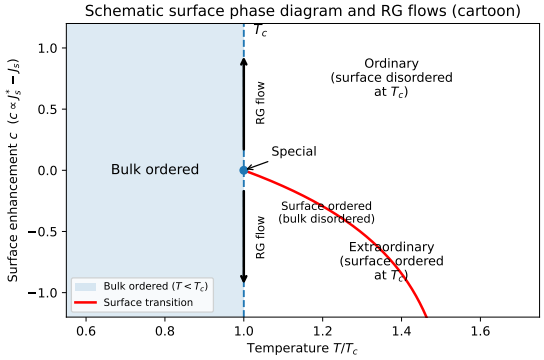

FIG. 1. Schematic surface phase diagram at fixed bulk criticality. The vertical axis is the surface scaling field $c - c^*$ (whose lattice realization is $J_s^* - J_s$ up to a positive prefactor; the figure axis is labeled c for brevity). The special fixed point is unstable in this direction; tuning $c - c^*$ drives the system toward ordinary ($c - c^* > 0$) or extraordinary ($c - c^* < 0$) surface behavior, with RG flow indicated.

II. CONTINUUM BENCHMARK

The semi-infinite Landau–Ginzburg action is

$$S[\phi] = \int_{z\ge 0} \mathrm{d}^d x \left[\tfrac{1}{2}(\nabla\phi)^2 + \tfrac{1}{2}\tau_0\phi^2 + \frac{u_0}{4!}\phi^4\right] + \int_{z=0} \mathrm{d}^{d-1}x_\parallel \, \tfrac{1}{2}c_0\phi^2. \tag{2}$$

Varying the surface term together with the integrated-by-parts bulk gradient term gives the Robin condition $\partial_z\phi|_{z=0} = c_0\phi|_{z=0}$ for the half-space convention used here. This sign is opposite to the outward-normal convention $\partial_n\phi = c\phi$ used in the Diehl literature (Ref. 1): with outward normal $\hat{n} = -\hat{z}$ on $z \ge 0$ (so $\partial_n = -\partial_z$), our c_0 equals $-c$ there. The physical side is anchored independently by the lattice: $J_s < J_s^*$ is the ordinary side (boundary disorders at bulk T_c), and the Green's function in Eq. (3) below confirms that positive c_0 in our

convention suppresses the boundary field — i.e. the ordinary regime. At bulk criticality, the Gaussian Green's function in mixed representation is, with $p = |\vec{p}_\parallel|$ the magnitude of the parallel momentum (the same object appears as p in Appendix A; in Appendix B, $\hat{q}$ is instead the internal loop momentum, distinct from the external p),

$$G(z, z'; p) = \frac{1}{2p}\left[\mathrm{e}^{-p|z-z'|} + \frac{p-c}{p+c}\mathrm{e}^{-p(z+z')}\right], \quad (3)$$

so the boundary structure factor is $S_{11}(p;c) = G(0,0;p) = 1/(p+c)$ and

$$R_G^{(k)}(p;c) = \frac{S_{11}(p;c)}{S_{11}(p;0)} = \frac{p}{p+c}. \quad (4)$$

The real-space boundary correlator is the two-dimensional Fourier transform of $1/(p+c)$. Using the Laplace representation $1/(p+c) = \int_0^\infty \mathrm{d}t\, \mathrm{e}^{-(p+c)t}$ gives

$$\begin{aligned} G_{11}(r;c) &= \frac{1}{2\pi r} F_G(cr), \\ F_G(s) &= \int_0^\infty \mathrm{d}u\, \mathrm{e}^{-su} \frac{u}{(1+u^2)^{3/2}}. \end{aligned} \quad (5)$$

Thus $(2\pi r)G_{11}(r;c) = F_G(cr)$ is the Gaussian one-parameter collapse used as a reference in the Monte Carlo plots. The limiting forms are $F_G(0) = 1$, giving $G_{11} \sim 1/(2\pi r)$ for $cr \ll 1$, and $F_G(s) \sim s^{-2}$ for $s \gg 1$, giving $G_{11} \sim 1/(2\pi c^2 r^3)$.

The important point is not that the interacting Ising curves should equal $F_G(s)$. They should not: anomalous dimensions change the scaling function. More precisely, in the interacting case the boundary correlator has the form $G_{11}(r;c) = r^{-(d-2+\eta_\parallel)}\mathcal{F}(r/\ell_c)$ with a nontrivial $\mathcal{F}$ that differs from F_G but shares its qualitative structure: monotone, one-parameter, exponentially decaying at large argument. The Gaussian solution gives an exactly solvable example of the crossover mechanism and a convenient operational template for extracting a single horizontal scale from noisy lattice ratios.

In the interacting $O(N)$ theory, translational invariance is broken and the surface enhancement must be renormalized independently. The relevant definitions are

$$\phi_s = (Z_\phi Z_1)^{1/2}\phi_{s,R}, \qquad c_0 - c_{\mathrm{sp},0} = \mu Z_c c, \quad (6)$$

where $c_{\mathrm{sp},0}$ is the nonuniversal bare special point. In minimal subtraction the bulk field renormalization is $Z_\phi = 1 + O(u^2)$, so it does not enter η_c at one loop and is suppressed in what follows. The one-loop surface two-point function has a boundary tadpole. In the boundary layer $z \to 0^+$ its singular pieces are controlled by

$$I_1(z) = \int_{\hat{q}} \frac{\mathrm{e}^{-2|\hat{q}|z}}{2|\hat{q}|}, \qquad I_2(z) = \int_{\hat{q}} \frac{\mathrm{e}^{-2|\hat{q}|z}}{\hat{q}^2}, \quad (7)$$

whose $d = 4 - \epsilon$ radial integrals generate the $1/\epsilon$ poles multiplying the boundary kinetic term and the surface enhancement. Minimal subtraction gives

$$Z_1 = 1 + \frac{N+2}{6}\frac{u}{\epsilon} + O(u^2), \qquad Z_c = 1 + \frac{N+2}{6}\frac{u}{\epsilon} + O(u^2). \quad (8)$$

Therefore

$$\begin{aligned} \eta_c(u) &= \mu\partial_\mu \ln Z_c = -\frac{N+2}{6}u + O(u^2), \\ \beta_c(c,u) &= -(1+\eta_c)c. \end{aligned} \quad (9)$$

At the Wilson–Fisher fixed point $u_* = 6\epsilon/(N+8)$,

$$y_c = 1 + \eta_c(u_*) = 1 - \frac{N+2}{N+8}\epsilon + O(\epsilon^2). \quad (10)$$

For Ising in $d = 3$, this gives the qualitative one-loop benchmark $y_c = 2/3$.[3, 4] The directly comparable precision values are the surface thermal eigenvalues at the special transition: $y_{t1}^{(s)} = 0.715(1)$ and $y_{ts} = 0.718(2)$,[5, 6] to which the one-loop $y_c = 2/3$ should be compared. Independent precision determinations of the *surface magnetic* dimension at the same fixed point are also available — $y_h = 1.646(2)$ for the special class from the boundary conformal bootstrap[11] and $\hat{\Delta}_\sigma = 0.3531(3)$ from improved-model Monte Carlo,[14] related by $y_h = (d-1) - \hat{\Delta}_\sigma$ in $d = 3$ — but these constrain a different operator sector and serve as orthogonal benchmarks of the surface CFT rather than direct checks on y_c. The $\sim 7\%$ gap between the one-loop $y_c = 2/3$ and $y_{t1}^{(s)} = 0.715(1)$ is qualitatively reasonable for an ϵ-expansion at $\epsilon = 1$; the dedicated two-loop fixed-dimension calculation with Borel resummation in Ref. 3 substantially closes it. The one-loop value is therefore best read as a qualitative benchmark rather than a precision prediction, and provides an independent reason to take the continuum framework as a reliable guide to the lattice analysis below. The equality $Z_1 = Z_c$ at one loop is structural at this order rather than accidental: both arise from the same pair of boundary tadpole integrals $I_{1,2}(z)$ in Eq. (7) with the same $(N+2)/6$ vertex combinatorics, and no other one-loop diagrams contribute to the boundary 1PI two-point function. The two structures split at higher loops, as the explicit two-loop calculation of Ref. 3 shows.

III. MONTE CARLO MODEL AND OBSERVABLES

We simulate spins $s_i = \pm 1$ on an $L \times L \times L_z$ simple-cubic slab with periodic in-plane boundaries and open normal boundaries. With $J = 1$,

$$\begin{aligned} H &= -\sum_{\langle ij \rangle} J_{ij} s_i s_j, \\ J_{ij} &= \begin{cases} J_s, & \text{surface in-plane bond,} \\ 1, & \text{otherwise.} \end{cases} \end{aligned} \quad (11)$$

Here J_s is the in-plane surface coupling; in the convention of Ref. 5, it corresponds to K_1/K, with $\kappa = K_1/K - 1$,

and the precision simple-cubic special point is at $\kappa_c = 0.50214(8)$, i.e. $K_1^*/K = 1.50214(8)$.[6] Wolff-cluster updates are performed at the bulk critical inverse temperature $\beta_c = 0.22165462(2)$.[8–10]

Three diagnostics are used. First, the surface magnetization and Binder cumulant,

$$m_1 = \frac{1}{L^2}\sum_{x,y} s_{x,y,z=0}, \qquad U_1 = 1 - \frac{\langle m_1^4\rangle}{3\langle m_1^2\rangle^2}, \tag{12}$$

locate the special region through

$$U_1(J_s; L, L_z) = \mathcal{U}((J_s - J_s^*)L^{y_c}, L_z/L) + \cdots, \tag{13}$$

where $\mathcal{U}$ is the universal surface-Binder scaling function (a function of the two dimensionless ratios shown, plus subleading scaling fields suppressed in the $\cdots$). Holding L_z/L fixed across sizes is what makes the cumulant intersections sharp; varying it instead — as in the simulations below — leaves a non-universal residue in the apparent crossing, which is the systematic the Results section returns to. Second, the surface susceptibility scales as $\chi_{11} \sim L^{\gamma_{11}/\nu}$ at special criticality, with $\gamma_{11}/\nu = 1 - \eta_\parallel$ in $d = 3$. Third, the direct surface correlator obeys $G_{11}(r) \sim r^{-(1+\eta_\parallel)}$ in the asymptotic regime. Surface correlations are measured from connected, translationally averaged top-layer correlators. On the ordinary side,

$$R_{\rm MC}(r; J_s) = \frac{G_{11}(r; J_s)}{G_{11}(r; J_s^*)} \tag{14}$$

is collapsed either with a threshold scale $R_{\rm MC}(\ell_{1/2}; J_s) = 1/2$ or with a one-parameter Gaussian-template scale $\ell_{\rm fit} = 1/c_{\rm fit}$. The simulations use $L = \{16, 24, 32\}$ at fixed $L_z = 32$, so aspect-ratio drift is a systematic limitation.

For susceptibility and direct-correlation diagnostics we use

$$\begin{aligned} \chi_{11} &= L^2\left(\langle m_1^2\rangle - \langle m_1\rangle^2\right), \\ G_{11}(r) &= \langle s(\mathbf{x}_\parallel, 0)s(\mathbf{0}, 0)\rangle_c. \end{aligned} \tag{15}$$

At the special transition $\chi_{11} \sim L^{\gamma_{11}/\nu}$ and $G_{11}(r) \sim r^{-(1+\eta_\parallel)}$ in $d = 3$, with $\gamma_{11}/\nu = 1 - \eta_\parallel$. These channels are not used to quote precision exponents, but they are useful checks on whether the working crossing estimate lands in the right scaling regime.

Errors on scalar observables are blocked jackknife. The Binder crossing is estimated by monotone-PCHIP interpolation and propagated by a Gaussian parametric bootstrap. For exponent-like fits, a bootstrap replicate is retained only if at least three ordinary-side length points survive after propagating J_s^* uncertainty; Gaussian-template scale fits are rejected if the optimizer hits imposed bounds.

IV. RESULTS

Binder crossings give the finite-size working estimate

$$J_s^* = 1.388 \pm 0.013, \tag{16}$$

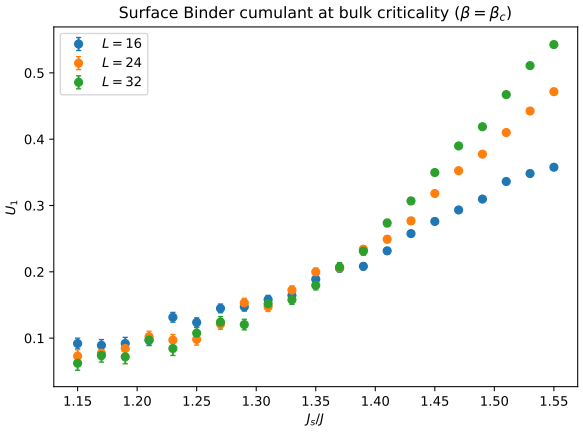

FIG. 2. Surface Binder cumulant U_1 versus surface coupling J_s for $L = 16, 24, 32$ at fixed $L_z = 32$. Blocked-jackknife error bars are smaller than the markers at this scale. The crossings give the finite-size working estimate $J_s^* = 1.388(13)$.

where the quoted uncertainty is statistical only; the dominant systematic, from aspect-ratio drift, is discussed below and is not folded in. This is roughly 9σ below — and $\sim 8\%$ smaller than — the precision simple-cubic value $K_1^*/K = 1.50214(8)$ quoted in Sec. III above.[5] A plausible leading cause is aspect-ratio drift: the simulations vary $L \in \{16, 24, 32\}$ at fixed $L_z = 32$, so L_z/L ranges from 2 at the smallest size down to 1 at the largest. The standard choice in precision surface MC is instead $L_z = 2L$ (Ref. 6 uses this), which costs only a constant factor in CPU time at each L but eliminates the aspect-ratio degree of freedom; the present project used the cheaper fixed-L_z schedule to keep the simulation envelope tractable. Surface Binder crossings are known to depend systematically on aspect ratio, and the dedicated precision study of Ref. 6 is careful to hold L_z/L fixed across sizes for exactly this reason. Subleading correction-to-scaling terms with surface irrelevant exponent ω_s may also contribute at these sizes, and the present data do not distinguish them from the aspect-ratio effect. We therefore treat $J_s^* = 1.388(13)$ as a finite-size working estimate, not as a new determination of the special point.

The consequence for what follows is uniform: every downstream universal-looking number in this section — γ_{11}/ν, $\eta_\parallel$, $y_c^{\rm app}$ — inherits this systematic. Each is informative about where the working crossing sits in the surface phase diagram, but none is an estimator of a special-point universal datum. With that caveat fixed, the positive structural result and the failure mode of the exponent fit can both be read off cleanly.

The strongest positive result is structural collapse. Figure 3 shows four real-space ratio curves collapsed by one horizontal scale each. Figure 4 repeats the test in momentum space using $S_{11}(p; J_s)/S_{11}(p; J_s^*)$. The dashed Gaussian curves are reference shapes, not the claimed interacting scaling functions; the evidence is that the data are

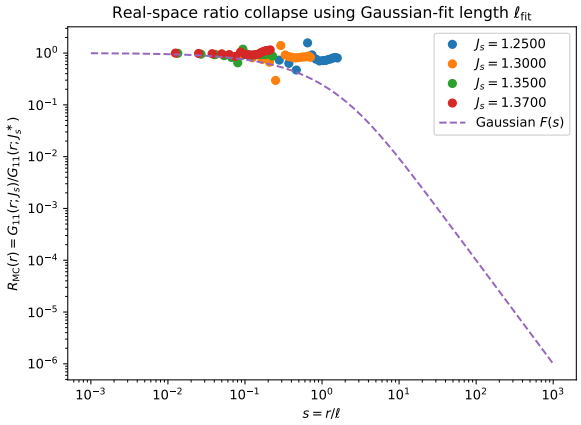

FIG. 3. Real-space ratio collapse for $R_{\rm MC}(r; J_s)$ on the ordinary side, plotted against $r/\ell_{\rm fit}(J_s)$. The four shown J_s curves are each rescaled by one horizontal parameter; the dashed Gaussian curve is the reference $F_G(s)$ from Eq. (5).

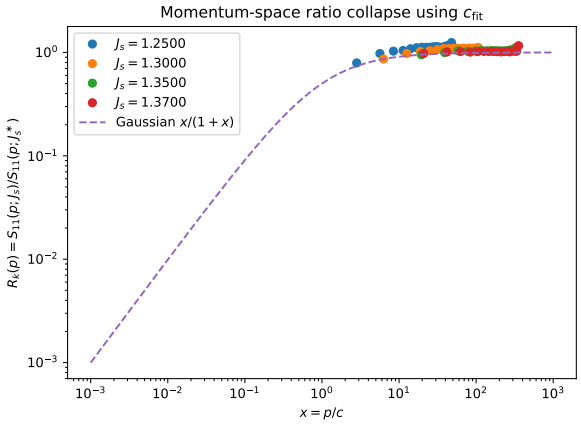

FIG. 4. Momentum-space ratio collapse $S_{11}(p; J_s)/S_{11}(p; J_s^*)$ plotted against $p/c_{\rm fit}(J_s)$. The dashed curve is the Gaussian $x/(1+x)$ form from Eq. (4).

organized by a single operational boundary length/scale.

A more conservative nonparametric version of the same test, using the threshold length $\ell_{1/2}$ defined by $R_{\rm MC}(\ell_{1/2}) = 1/2$, is shown in Fig. 7 of Appendix C. It loses curves because the ratio must actually cross one half inside the finite radial window, so only two J_s values qualify; the resolved curves are consistent with, but do not independently demonstrate, the same one-parameter organization.

A rough second channel is consistent with the same finite-size limitation: the three-point susceptibility fit at the nearest grid point gives $\gamma_{11}/\nu \simeq 0.96$, far from the special-transition literature value near 0.625.[6] Direct real-space and momentum-space estimates of $\eta_\parallel$ also disagree strongly (Appendix C), so we do not quote them as exponents.

The pattern across channels is informative and is summarized in Table I. Operationally, the location-like observable J_s^* saturates gracefully under finite size while the local-slope estimators saturate catastrophically, and they do so in mutually inconsistent directions (the two $\eta_\parallel$ estimators do not even agree in sign). This is the same statement as Eq. (18) read across channels: any quantity that requires resolving the slope of a near-saturated curve fails in the same way for the same reason, which is why the slope-like estimators are all wrong and the location-like estimator is only moderately wrong.

TABLE I. Cross-channel summary of fit outputs and their literature counterparts. J_s^* is location-like (integrated/extremum estimator); the rest are slope-like. The hierarchy of relative deviations — $\sim 8\%$ on the location, tens of percent and sign-inconsistent on the slopes — is the same statement as Eq. (18) read channel by channel.

channel	this work	literature	relative
J_s^*	1.388(13)	1.50214(8)[6]	-8%
γ_{11}/ν	$\simeq 0.96$	$\simeq 0.625$[6]	$+54\%$
$\eta_\parallel$ (real)	$\simeq 0.586$	≈ 0.37[6]	$+58\%$
$\eta_\parallel$ (mom.)	$\simeq -0.255$	≈ 0.37	sign-wrong
$y_c^{\rm app}$, working anchor	$\simeq 4.95$	≈ 0.72[6]	$\times 6.9$
$y_c^{\rm app}$, literature anchor	$\simeq 1.55$	≈ 0.72	$\times 2.2$

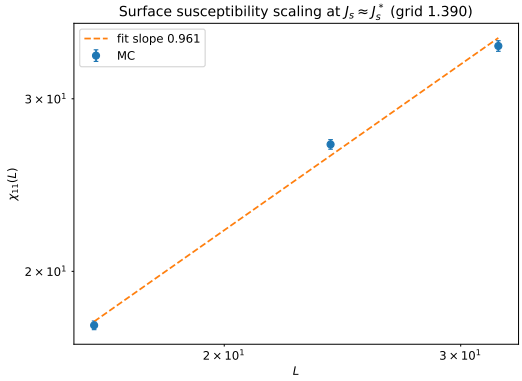

FIG. 5. Surface susceptibility scaling at the nearest grid point to J_s^*. The fitted three-point slope is about 0.96, while the special-transition literature value is $\gamma_{11}/\nu \simeq 0.625$;[6] this is another sign that the finite-size crossing is not yet an asymptotic special-point estimate.

The exponent extraction from $\ell(J_s)$ fails. A clean infinite-volume power law requires $1 \ll \ell_c(\Delta_s) \ll L$, or equivalently $L^{-y_c} \ll \Delta_s \ll 1$, with $\Delta_s = J_s^* - J_s$ linearly related to the continuum scaling field $c - c^*$ near the special point up to subleading analytic corrections. Numerically, $y_c \approx 0.72$ and $L = 32$ give $L^{-y_c} \approx 0.08$, so the fit window requires Δ_s comfortably above ~ 0.08 and small compared to 1. Using the working $J_s^* = 1.388$, the four ordinary-side points span $\Delta_s \in [0.018, 0.138]$, which sits on or below the lower edge of the window; using the literature $J_s^* \simeq 1.502$, they span $\Delta_s \in [0.132, 0.252]$, which is

TABLE II. Exponent-fit diagnostics from the five-seed $L = 32$ synthesis. "Valid boots" counts bootstrap resamples in which a fit could be performed at all, not a sample of a parameter posterior; the small fraction reflects how close the data sit to saturation. The literature-anchor row is a deterministic refit of the same four $\ell_{1/2}(J_s)$ values with only the subtraction point changed. The apparent numbers are failure diagnostics, not universality estimates.

channel	valid boots	result
$\ell_{1/2}$ threshold	13/3000	$y_c^{\rm app} = 4.95(6)$
same $\ell_{1/2}$, $J_s^* = 1.50214$	deterministic	$y_c^{\rm app} = 1.55$
Gaussian scale	0/3000	bound-hit rejection

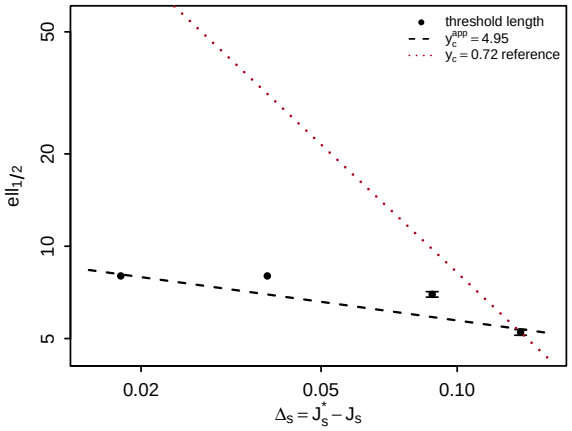

FIG. 6. Threshold length $\ell_{1/2}$ versus $\Delta_s = J_s^* - J_s$. The black dashed line is the finite-window trend from the few surviving bootstrap fits and is dominated by the saturated near-special points. The red dotted line shows the much steeper slope expected from $y_c \simeq 0.72$, anchored at the largest Δ_s point.

narrow and shifted toward the upper edge. Neither range supports an asymptotic power law. The current data sit close to saturation near the special point. Differentiating

$$\ell = A\Delta_s^{-1/y_c}\left[1 + B\Delta_s^{\omega_s/y_c} + \cdots\right] \tag{17}$$

gives

$$\frac{1}{y_c^{\rm app}} \equiv -\frac{\partial \log \ell}{\partial \log \Delta_s}\Big|_{\rm fit} \approx \frac{1}{y_c} - \frac{B\omega_s}{y_c}\Delta_s^{\omega_s/y_c} + O(L^{-\omega_s}), \tag{18}$$

so local slopes are sensitive to corrections and to uncertainty in the subtraction defining Δ_s.

Only 13 of 3000 threshold bootstraps pass the minimum-data criterion, and the Gaussian-template length yields no valid draws after bound-hit filtering (Table II). The surviving threshold fits cluster near $y_c^{\rm app} \simeq 4.95$, roughly seven times the known Ising value. Holding the same four operational $\ell_{1/2}(J_s)$ values fixed but re-anchoring the scaling-field subtraction at the literature value $J_s^* = 1.50214$ gives $\Delta_s \in [0.132, 0.252]$ and a direct log-log fit slope -0.647, i.e. $y_c^{\rm app} = 1.55$. This is still far from 0.72, although much less pathological than 4.95, so it confirms that the exponent failure is not just an artifact of the working crossing subtraction. The data show one-parameter crossover structure, but not a resolved asymptotic slope.

The failure mode is physically unsurprising, and the magnitudes are larger than corrections-to-scaling alone would explain. For $y_c^{\rm app}$: the threshold $\ell_{1/2}$ is itself clipped by the finite radial window for the smallest-Δ_s curves — the ratio $R_{\rm MC}$ does not cross 1/2 until r comparable to or exceeding the in-plane size $L = 32$, so $\ell_{1/2}$ saturates to a finite-window value rather than the diverging $\ell_c(\Delta_s)$. The slope $\partial \log \ell / \partial \log \Delta_s$ is then being read off a near-flat region, not a power law, which can produce an essentially arbitrary apparent exponent. The working-anchor fit's factor-of-seven discrepancy decomposes into a factor of about 3 from the misplaced Δ_s subtraction (4.95/1.55) and a residual factor of about 2 from finite-window saturation under the literature anchor (1.55/0.72). The latter is still much too large for Eq. (18) treated as a small correction-to-scaling perturbation. The sign flip in the momentum-space $\eta_\parallel$ fit has a similar origin: at the special point $S_{11}(p)$ crosses over between two power-law regimes near $p \sim 1/L$, and a three-point fit straddling the crossover can extract either slope or worse. The apparent exponent therefore reports the finite-window geometry of the analysis, not a surface universality class.

V. CONCLUSION

The continuum theory, one-loop RG, and slab data give a coherent but limited result. The Monte Carlo ratios show the expected one-parameter boundary crossover, and Binder crossings locate a plausible finite-size special region. The same data do not determine y_c: the apparent exponent is far from the known 0.715–0.718 range and survives only under severe bootstrap selection. A precision campaign would need, in roughly this order of importance, larger L (at least the $L \gtrsim 64$ scale used in precision surface studies,[6, 12] which is the only way to open an asymptotic window in Δ_s), fixed aspect ratio L_z/L (the leading candidate among several plausible causes of the present J_s^* shift), a denser grid near J_s^*, and explicit correction-to-scaling fits.

ACKNOWLEDGMENTS

N.A. thanks Mehran Kardar for a great semester, and Zixia Wei, Raphael Dulac, and Mengyang Zhang for being a wonderful collaborator on a paper which loosely inspired this project.

Appendix A: Derivations for the continuum formulas

Varying Eq. (2) under $\phi \mapsto \phi + \delta\phi$ gives the boundary contribution

$$\delta S_{\partial V} = \int_{\partial V} \mathrm{d}^{d-1}x_{\parallel}\,(\partial_n\phi + c_0\phi)\delta\phi. \tag{A1}$$

For the half-space $z \geq 0$, the outward normal is $-\hat{z}$, so this is equivalently $\partial_z\phi = c_0\phi$ at $z = 0$.

The Gaussian propagator follows from the mixed-representation boundary-value problem

$$(-\partial_z^2 + p^2)\widetilde{G}(p; z, z') = \delta(z - z'), \qquad (\partial_z - c_0)\widetilde{G}|_{z=0} = 0. \tag{A2}$$

The decaying solution is a free Green's function plus one image term. Continuity at $z = z'$, the derivative jump condition, and the Robin condition fix it uniquely:

$$\widetilde{G}(p; z, z') = \frac{1}{2p}\left[\mathrm{e}^{-p|z-z'|} + \frac{p - c_0}{p + c_0}\mathrm{e}^{-p(z+z')}\right]. \tag{A3}$$

Setting $z = z' = 0$ gives $S_{11}(p; c) = 1/(p + c)$ and Eq. (4).

For the real-space formula, insert $1/(p + c) = \int_0^\infty \mathrm{d}t\,\mathrm{e}^{-(p+c)t}$ into the two-dimensional Fourier transform. The angular integral and the identity

$$\int_0^\infty \mathrm{d}p\,p\,\mathrm{e}^{-tp}J_0(pr) = \frac{t}{(t^2 + r^2)^{3/2}} \tag{A4}$$

give

$$G_{11}(r; c) = \frac{1}{2\pi}\int_0^\infty \mathrm{d}t\,\mathrm{e}^{-ct}\frac{t}{(t^2 + r^2)^{3/2}}. \tag{A5}$$

Changing variables $t = ru$ yields Eq. (5). The limits $F_G(0) = 1$ and $F_G(s) \sim s^{-2}$ follow by direct integration and Laplace's method.

Appendix B: Boundary one-loop pole structure

The one-loop surface exponent follows from the 1PI surface two-point function. At tree level $\Gamma^{(0)}_{11,0}(\hat{p}) = |\hat{p}| + c_0$. The one-loop correction is a tadpole inserted between two boundary-to-bulk propagators,

$$\delta G_{11,0}(\hat{p}) = -\int_0^\infty \mathrm{d}z\,G_0(\hat{p}; 0, z)\Sigma_0(z)G_0(\hat{p}; z, 0), \tag{B1}$$

with $\Sigma_0(z) = (N + 2)u_0\int_{\hat{q}} G_0(\hat{q}; z, z)/6$. The UV singularity comes from large $|\hat{q}|$ and $z \to 0^+$. Expanding

$$G_0(\hat{q}; z, z) = \frac{1}{2|\hat{q}|}\left[1 + \frac{|\hat{q}| - c_0}{|\hat{q}| + c_0}\mathrm{e}^{-2|\hat{q}|z}\right] \tag{B2}$$

gives the boundary-layer structures in Eq. (7). Their radial integrals have singular behavior

$$I_1(z) \sim \frac{1}{16\pi^2\epsilon^2}, \qquad I_2(z) \sim \frac{1}{4\pi^2\epsilon^{1-\epsilon}}, \tag{B3}$$

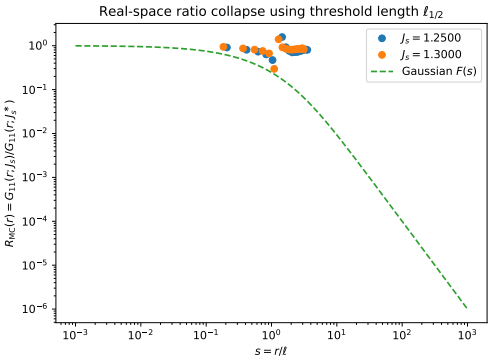

FIG. 7. Real-space ratio collapse using the threshold length $\ell_{1/2}$ defined by $R_{\mathrm{MC}}(\ell_{1/2}) = 1/2$. This nonparametric extractor is more conservative than the Gaussian-template scale used in Fig. 3 and loses near-special points when the ratio does not cross one half inside the finite radial window.

and the remaining z integrals produce $\Gamma(\epsilon - 1)$ and $\Gamma(\epsilon)$ poles. After the additive shift defining $c_{\mathrm{sp},0}$, the pole terms are proportional to the same two boundary structures already present at tree level, $|\hat{p}|$ and c. This gives Eq. (8) and hence Eq. (10).

Appendix C: Monte Carlo and fit diagnostics

For inhomogeneous ferromagnetic couplings, the Wolff update uses the local bond probability $p_{ij} = 1 - \mathrm{e}^{-2\beta J_{ij}}$. Detailed balance is the standard cluster argument with J replaced by J_{ij} bond by bond: boundary bonds omitted from the cluster contribute factors $\mathrm{e}^{-2\beta J_{ij}}$ when satisfied, and the ratio of forward and reverse cluster-generation probabilities is exactly $\mathrm{e}^{-\beta\Delta H}$.

Errors are blocked jackknife with block size 50 for measured observables. Binder-crossing uncertainty is propagated by a Gaussian parametric bootstrap of $U_1(J_s; L)$ values with monotone-PCHIP interpolation of the crossing. For exponent-like fits, a bootstrap draw is retained only if at least three ordinary-side points survive after propagating the crossing uncertainty; Gaussian-template scale fits are additionally rejected when the optimizer hits imposed bounds. As a robustness check, threshold lengths $\ell_{1/2}$ extracted at $L = 24$ and $L = 32$ agree within errors at the two resolved Δ_s values; points closer to J_s^* are unresolved in both sizes, which is why exponent extraction fails identically in either.

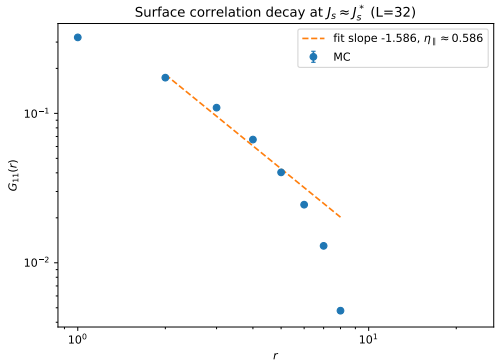

FIG. 8. Illustrative real-space fit of $G_{11}(r) \sim r^{-(1+\eta_\parallel)}$ near J_s^*. The fitted $\eta_\parallel \simeq 0.586$ is far from both the momentum-space estimate in Fig. 9 and the special-transition literature value $\eta_\parallel \approx 0.37$,[6] indicating contamination from finite-size and lattice-window effects.

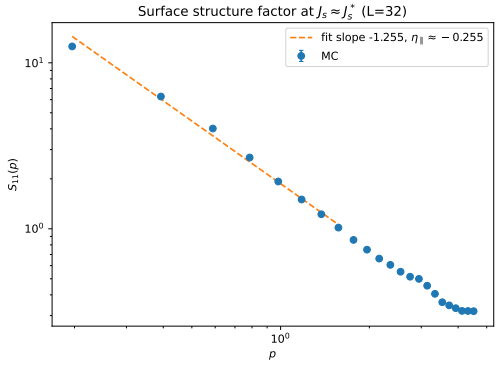

FIG. 9. Illustrative momentum-space fit of $S_{11}(p) \sim p^{\eta_\parallel - 1}$ near J_s^*. The fitted $\eta_\parallel \simeq -0.255$ disagrees with Fig. 8 and with the literature value $\eta_\parallel \approx 0.37$; neither fit is used as a quoted exponent.

[1] H. W. Diehl, "The theory of boundary critical phenomena," Int. J. Mod. Phys. B **11**, 3503 (1997), arXiv:cond-mat/9610143.

[2] K. Binder, "Critical behavior at surfaces," in *Phase Transitions and Critical Phenomena*, Vol. 8, edited by C. Domb and J. L. Lebowitz (Academic Press, 1983).

[3] H. W. Diehl and M. Shpot, "Massive field-theory approach to surface critical behavior in three-dimensional systems," Nucl. Phys. B **528**, 595 (1998), arXiv:cond-mat/9804083.

[4] H. W. Diehl and S. Dietrich, "Field-theoretical approach to multicritical behavior near free surfaces," Phys. Rev. B **24**, 2878(R) (1981).

[5] Y. Deng, H. W. J. Blote, and M. P. Nightingale, "Surface and bulk transitions in three-dimensional $O(n)$ models," Phys. Rev. E **72**, 016128 (2005), arXiv:cond-mat/0504173.

[6] M. Hasenbusch, "A Monte Carlo study of surface critical phenomena: The special point," Phys. Rev. B **84**, 134405 (2011), arXiv:1108.2425.

[7] J. L. Cardy, "Conformal invariance and surface critical behavior," Nucl. Phys. B **240**, 514 (1984).

[8] U. Wolff, "Collective Monte Carlo Updating for Spin Systems," Phys. Rev. Lett. **62**, 361 (1989).

[9] R. H. Swendsen and J.-S. Wang, "Nonuniversal critical dynamics in Monte Carlo simulations," Phys. Rev. Lett. **58**, 86 (1987).

[10] M. Hasenbusch, "Finite size scaling study of lattice models in the three-dimensional Ising universality class," Phys. Rev. B **82**, 174433 (2010).

[11] F. Gliozzi, "Truncatable bootstrap equations in algebraic form and critical surface exponents," JHEP **10**, 037 (2016), arXiv:1605.04175.

[12] F. Parisen Toldin, "Boundary Critical Behavior of the Three-Dimensional Heisenberg Universality Class," Phys. Rev. Lett. **126**, 135701 (2021), arXiv:2012.00039.

[13] M. A. Metlitski, "Boundary criticality of the $O(N)$ model in $d = 3$ critically revisited," SciPost Phys. **12**, 131

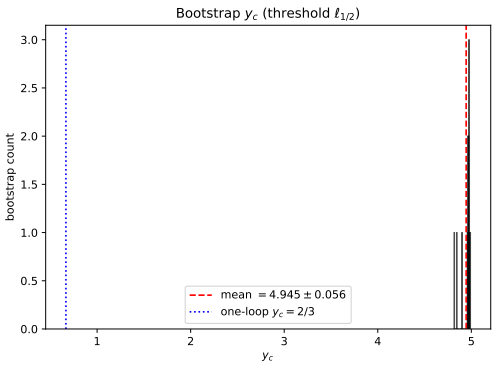

FIG. 10. Bootstrap distribution for the threshold-based apparent exponent. Only 13/3000 replicates satisfy the minimum-data criterion, so the histogram is an instability diagnostic rather than a precision estimate.

(2022), arXiv:2009.05119.

[14] D. Przetakiewicz, S. Wessel, and F. Parisen Toldin, "Boundary operator product expansion coefficients of the three-dimensional Ising universality class," arXiv:2502.14965 (2025).